

pubs.acs.org/acscatalysis Research Article

# The Role of the Unusual 2-Tyr-1-carboxylate Nonheme Iron Motif in the Mechanism of N,N-Dimethylformamidase

David W. Kastner, Clorice R. Reinhardt, Husain Adamji, Terence S. Oscar-Okpala, Ilia Kevlishvili, Yuriy Román-Leshkov, and Heather J. Kulik\*



Cite This: ACS Catal. 2025, 15, 12822-12834



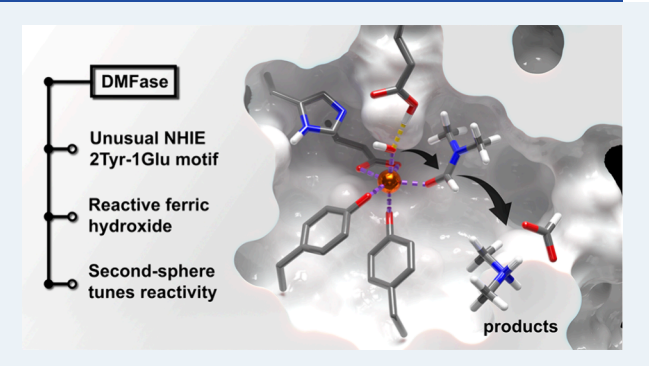
**ACCESS** I

III Metrics & More

Article Recommendations

SI Supporting Information

ABSTRACT: N,N-Dimethylformamidase (DMFase) is a nonheme iron enzyme that catalyzes the hydrolysis of N,N-dimethylformamide (DMF) using a noncanonical Fe(III)-2Tyr-1Glu coordination motif. The precise role that this nonconventional active site plays in catalysis remains poorly understood. We performed an extensive computational investigation of DMFase catalysis, combining reaction pathway analysis with quantum mechanical cluster models, charge shift analysis, and energy decomposition analysis to identify the mechanistic role of the coordinating tyrosines/glutamate and second coordination sphere residues. We compared two mechanisms initiated by the key second coordination sphere residues Glu657 and His519. While both mechanisms generate a ferric hydroxide intermediate, the Glu657-



initiated mechanism exhibits more favorable barriers and thermodynamics. These calculations reveal distinct catalytic roles for the second-sphere residues: Glu657 facilitates direct proton transfers, His519 and Asn547 stabilize the rate-determining transition state, and Lys567 stabilizes the anionic tyrosinate state of Tyr440. Mechanistic comparisons to canonical Fe(II)/Fe(III)-2His-1Glu variants reveal that coordination of Fe by tyrosine residues lowers the barrier for deprotonation of a water ligand and subsequent nucleophilic attack on DMF. Attempts to tune the active site through fluorination of coordinating tyrosinate residues yield minimal additional benefits, indicating that the native motif has finely tuned electronic characteristics. These results demonstrate how the 2Tyr-1Glu motif and its second coordination sphere context enable hydrolytic reactivity in DMFase and suggest Glu657 and Lys567 as targets of future mutagenesis to validate their mechanistic roles.

KEYWORDS: metalloenzyme, quantum chemistry, electrostatics, amidohydrolase, nonheme iron, bioremediation, density functional theory, reaction mechanism

### 1. INTRODUCTION

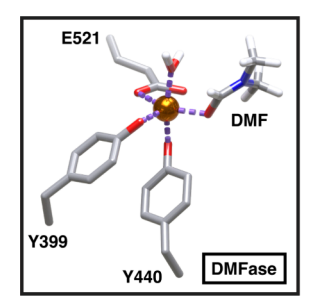
Enzymes isolated from microbes inhabiting polluted environments have attracted attention for their ability to degrade anthropogenic compounds such as plastics, 1-5 aromatic amines,6 and industrial solvents.7,8 While certain bioremediation enzymes have evolved novel active site configurations such as the fused flavodoxin-P450 XplA system involved in the degradation of RDX explosives<sup>9</sup>—the majority utilize wellestablished, canonical structural motifs. 10 One intriguing exception is N,N-dimethylformamidase (DMFase), a nonheme iron enzyme whose Fe(III) center is coordinated by two tyrosinate residues and one glutamate (2Tyr-1Glu). This unusual coordination motif enables DMFase to hydrolyze the industrial solvent N,N-dimethylformamide (DMF). <sup>11-13</sup> This configuration in DMFase deviates from the canonical 2histidine-1-carboxylate (2His-1Asp/Glu) motif that characterizes the majority of nonheme iron enzymes. 14,15

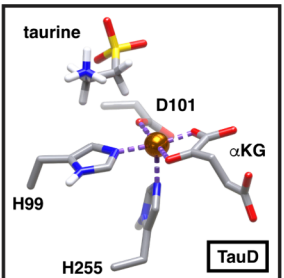
There are several subclasses of 2His-1Asp nonheme iron enzymes (NHIEs), such as  $\alpha$ -ketoglutarate-dependent dioxygenases, Rieske dioxygenases, and extradiol dioxygenases

nases,<sup>21</sup> that have been extensively studied, including for their bioremediation potential. Canonical NHIEs typically catalyze oxidative transformations, including hydroxylation,<sup>22–25</sup> halogenation,<sup>26,27</sup> epoxidation,<sup>28</sup> azidation,<sup>29</sup> and isonitrile formation,<sup>30,31</sup> whereas DMFase catalyzes a hydrolytic reaction, cleaving the C–N bond of DMF.<sup>32</sup> The distinctive Fe(III)-2Tyr-1Glu coordination environment in DMFase, coupled with purported direct substrate binding to the iron center, suggests a catalytic mechanism fundamentally different from that of conventional hydroxylase and halogenase NHIEs (Figure 1). However, the electronic effects of this noncanonical first-sphere coordination and its role in direct substrate binding are challenging to characterize through experimental meth-

Received: May 16, 2025 Revised: June 23, 2025 Accepted: June 27, 2025







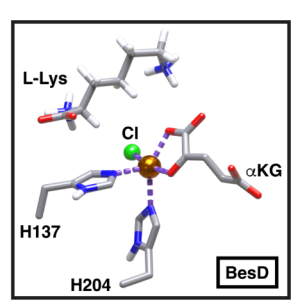


Figure 1. Comparison of the DMFase coordinating residues and substrate position to that of a nonheme iron hydroxylase and halogenase. (left) DMFase active site (PDB: 6LVV) with modeled DMF. (middle) Active site of the hydroxylase TauD (PDB: 1GY9). (right) Active site of halogenase BesD (PDB: 6NIE). Atoms are colored as follows: carbon, gray; nitrogen, blue; oxygen, red; sulfur, yellow; chlorine, green; hydrogen, white; and iron, dark orange. Coordinating bonds are shown as purple dashed lines.

ods.<sup>33</sup> To address these limitations, computational methods such as quantum mechanical (QM) calculations<sup>34</sup> and molecular dynamics (MD) simulations<sup>35</sup> or coupled QM/MM simulations<sup>36</sup> have emerged as powerful tools,<sup>37–41</sup> providing atomic-level insight into active-site reactivity.<sup>41–44</sup> Computational approaches have proven valuable for examining unusual metal coordination geometries of nonheme iron enzymes (e.g., SyrB2<sup>45,46</sup> and CDO<sup>47–49</sup>), elucidating subtle electronic effects arising from ligand identity<sup>50</sup> and substrate positioning.<sup>51–57</sup> These methods have also guided the rational engineering of a number of bioremediation enzymes<sup>58,59</sup> (e.g., DhaA,<sup>60</sup> LinB,<sup>61</sup> FAcD,<sup>62</sup> and PTE<sup>63</sup>).

While there are no comprehensive computational studies on the full mechanism of DMFase, structural and mutagenesis studies have begun to illuminate the unusual active site of DMFase. Specifically, X-ray crystallography and cryogenic electron microscopy have detailed the unique 2Tyr-1Glu iron coordination of DMFase. 13,64 Second coordination sphere residues His519 and Asn547 have been shown to be essential for catalytic activity through site-directed mutagenesis studies. 13 However, despite these structural insights, the detailed catalytic mechanism of DMFase, particularly the C-N bond cleavage step, remains poorly understood.<sup>65</sup> A mechanism previously suggested based on static crystal structures proposed DMF substrate coordination to Fe(III), followed by nucleophilic attack from an unbound water molecule, with His519 serving as a general base and supported by Asn547.<sup>13</sup> Preliminary computational studies investigated active-site strain and gas-phase nonenzymatic reaction energetics, 13 but a comprehensive computational examination of the full catalytic cycle of DMFase has not been carried out.

To bridge these gaps in understanding, we conducted detailed QM modeling investigations of the Fe(III)-2Tyr-1Glu active site in DMFase, specifically exploring two distinct catalytic mechanisms initiated by either Glu657 or His519 and contrasting them with the nonenzymatic hydrolysis of DMF in water. We also examined the contributions of the second coordination sphere residues His519, Asn547, and Lys567 to the stabilization of key transition states. To further elucidate the role of Tyr residues in catalytic action, we contrasted reaction coordinates evaluated with Fe(II) or Fe(III) 2His-1Glu active sites as well as those in which the Tyr residues are fluorinated. These findings provide atomic-level insight into how contributions from the first- and second-coordinationsphere residues enable DMFase reactivity, offering a blueprint for developing engineered NHIEs with hydrolytic function using the unique 2Tyr-1Glu motif.

# 2. COMPUTATIONAL DETAILS

**2.1. QM Cluster Model Preparation.** To investigate the reactivity of DMFase, we constructed multiple QM cluster models based on chain A of the  $\beta$ -subunit from the crystal structure (PDB: 6LVV). 13 The Glu657-initiated and His519initiated mechanisms were modeled by using a 174-atom QM cluster with a net charge of 0. This model included the Fe(III) center, DMF, the coordinating water molecule, the primary coordination sphere residues Tyr399, Tyr440, and Glu521, as well as the second coordination sphere residues His519, Tyr522, Asn547, Lys567, and Glu657 (Supporting Information Table S1). Protonation states for His519 and Glu657 were assigned using H++ at pH 7.0 ( $\varepsilon$  = 10). This returned His519 in the neutral N $\delta$ 1-protonated tautomer (HID), which was used for all subsequent calculations (Supporting Information Table S2). DMF was placed in the open coordination site, using the same coordinates as the MD simulations, with the carbonyl oxygen of DMF coordinating iron, leaving the bound water in its original coordination site. All residues were included with their full backbones and side chains, and backbone atoms were fixed in space during geometry optimizations to preserve the crystallographic geometry of the protein fold. The selection of second coordination sphere residues was guided by charge shift analysis (CSA)<sup>66,67</sup> to identify residues that undergo significant charge redistribution upon removal of the core active site (Supporting Information Texts S1-S3). CSA calculations were performed on QM/MM single-point calculations using representative structures clustered from six independent 250 ns MD simulations, each for the holoenzyme and apoenzyme (totaling 3  $\mu$ s, Supporting Information Text S1). We used only the ferric, Fe(III), oxidation state for MD parametrization, consistent with experimental paramagnetic resonance data indicating an Fe(III) resting state.<sup>13</sup> The possibility of redox activity was not modeled and remains a limitation. Residues exhibiting a charge shift ( $\Delta q_{RES} \ge |0.05 e|$ ) were incorporated into the QM model (Supporting Information Text S3). In the Glu657initiated and His519-initiated mechanisms, iron was modeled in the +3 oxidation state, consistent with experimental paramagnetic resonance data. 13,68,69 Localized orbital bond analysis (LOBA),<sup>70</sup> as implemented in Multiwfn,<sup>71</sup> confirmed the Fe(III) oxidation state remained unchanged throughout the reaction mechanism. The QM cluster models were evaluated in both the high-spin sextet multiplicity (2S + 1)6) and the low-spin doublet multiplicity (2S + 1 = 2)(Supporting Information Figure S1). Additional QM cluster models were constructed to probe active site modifications.

These models were built using the original cluster model, retaining the same initial second sphere residues but also including: a histidine-substituted variant of the active site (replacing Tyr399 and Tyr440 with histidines), and a 3,5difluorotyrosinate-substituted variant. In addition, two reduced models were constructed: a minimal model isolating the Lys567-Tyr440 cation- $\pi$  interaction, and a nonenzymatic model containing only DMF and five explicit water molecules (Supporting Information Table S1 and Figure S2). In addition to the minimal model isolating the Lys567–Tyr440 cation– $\pi$ interaction, a more complete model containing Tyr399, Tyr440, His519, Glu521, Asn547, Lys567, and Glu657 was also constructed. To investigate the potential stabilization of Tyr399 by Trp473, this large, iron-free model was further modified to include Trp473. The histidine-substituted model was generated by aligning the DMFase active site with that of TauD (PDB: 1OS7),68 after which the introduced histidines were geometry-optimized at the QM level (see Section 2.2) with backbone atoms restrained.

2.2. Quantum Mechanical Calculations and Analysis. All QM calculations were performed using ORCA version Geometry optimizations were carried out at the B3LYP-D3/LACVP\* level of theory, which corresponds to the LANL2DZ effective core potential applied to iron and 6-31G\* applied to the other atoms. Empirical dispersion corrections were included using the DFT-D3 semiempirical correction<sup>76</sup> with Becke-Johnson damping.<sup>77</sup> Gibbs free energy corrections were applied to all optimized intermediates and transition states, computed at 298.15 K. Frequency calculations were carried out to confirm that intermediates exhibited no imaginary frequencies and that transition states contained a single imaginary frequency corresponding to the expected reaction coordinate. All QM calculations were performed in implicit solvent using the conductor-like polarizable continuum model (C-PCM) with a dielectric constant  $(\varepsilon)$  of 10, chosen to approximate the electrostatic environment of the protein active site. 78,79 The solute cavity was constructed using 1.2 × Bondi radii for all elements, as implemented in ORCA.<sup>72</sup> For the nonenzymatic reaction calculations, a dielectric constant of  $\varepsilon$  = 80 was used to approximate an aqueous environment. 79 Reaction pathways were determined using climbing image nudged elastic band (CI-NEB) calculations starting from an interpolated path between geometry-optimized intermediates. The intermediates used as end states for these NEB calculations were first identified based on chemical intuition of the multistep reaction and subsequently confirmed as stable minima through unconstrained geometry optimizations. All CI-NEB calculations used a minimum of 48 images, although specific steps, where noted, used as many as 72 images to resolve the reaction coordinate. The default spring constants were applied. The maximum-energy structures from NEB calculations were then refined using partitioned rational function optimization (P-RFO)<sup>80</sup> to locate transition states. Single-point energy calculations were performed for all optimized intermediates and transition states using the B3LYP/def2-TZVPP and B3LYP/def2-QZVPP basis sets. The resulting energies were extrapolated to the complete basis set (CBS) limit using a twopoint extrapolation formula. 81,82 To assess functional sensitivity, single-point energy calculations were also conducted at the PBE/LACVP\*, 83 PBE0/LACVP\*, 84,85 and ωB97X/ LACVP\*86 levels of theory for all intermediates and transition states (Supporting Information Tables S8 and S11).

Electronic structure analysis was performed using quantum theory of atoms in molecules (QTAIM) to identify bond critical points (BCPs)<sup>87</sup> and quantify hydrogen bonding interactions based on the potential energy density of the closest BCP. 88-90 The bond valence of coordinating interactions was computed using Multiwfn.71 To further decompose the electronic contributions governing reactivity, absolutely localized molecular orbital (ALMO) energy decomposition analysis (EDA)<sup>91</sup> was conducted in Q-Chem version 6.092 for all optimized intermediates and transition states. Complementary occupied-virtual pair (COVP) analysis was employed to interpret the charge-transfer component of ALMO-EDA in terms of fragment-localized donor-acceptor orbital interactions and was also performed in Q-Chem. NEB calculations were performed for the first five steps of the reaction mechanism for these models to capture the ratedetermining step. In the case of the QM cluster model with substituted coordinating histidines, the reaction was modeled separately with either an Fe(II) or Fe(III) oxidation state, as Fe(II) is the resting state commonly observed in 2His-1carboxylate nonheme iron enzymes, whereas Fe(III) is more consistent with observations on the native DMFase active site.93

#### 3. RESULTS AND DISCUSSION

3.1. Evaluation of Reaction Mechanisms. To investigate the mechanistic role of the nonheme iron 2Tyr-1Glu motif of DMFase and its second coordination sphere residues in the hydrolysis of dimethylformamide (DMF), we first evaluated the nonenzymatic hydrolysis of DMF under aqueous conditions. We refer to this as mechanism one and use the superscript 1 to distinguish this mechanism (e.g., <sup>1</sup>TS<sub>2</sub> is the second TS in this mechanism and <sup>1</sup>IM<sub>3</sub> is the third intermediate, where the subscript refers to the number of the step in the reaction coordinate). This allowed us to determine the upper bound of the energetics for DMF hydrolysis in an enzyme. To model the nonenzymatic reaction, we included a network of five explicit water molecules in addition to an implicit solvent environment around these waters. We created a water cluster around DMF in the reactant state (1R), and we selected a total of five waters because we believed it was a sufficient number of waters to stabilize a hydroxide through a series of proton transfers, as suggested experimentally (Figure 2 and Supporting Information Figures S7-S9). 94,95 All reported free energies  $(\Delta G)$  are referenced to this initial reactant state, unless specified otherwise. The reaction is initiated with a concerted step in which proton transfers between water molecules lead to the protonation of the amine of DMF and generate the reactive hydroxide. The reactive hydroxide attacks the carbonyl carbon with a <sup>1</sup>TS<sub>1</sub> barrier of  $\Delta G^{\ddagger}$  = 32.0 kcal/mol (Figure 2 and Supporting Information Tables S5, S6). This high barrier represents the ratedetermining step and is consistent with the lack of spontaneous hydrolysis of DMF in water. Nucleophilic attack by the hydroxide triggers spontaneous cleavage of the C-N bond, producing dimethylamine and formic acid, with a computed free energy of  $\Delta G = 9.9 \text{ kcal/mol for }^{1}\text{IM}_{2}$  (Figure 2). The products are then generated with a  $\Delta G^{\ddagger}$  of 13.4 kcal/mol relative to the reactants after a final proton transfer between formic acid and dimethylamine to produce the formate and dimethylammonium products ( ${}^{1}\mathbf{P}$ ) at  $\Delta G = -6.5$  kcal/mol relative to the reactant state (Figure 2 and Supporting Information Figure S10). The high barriers observed in these

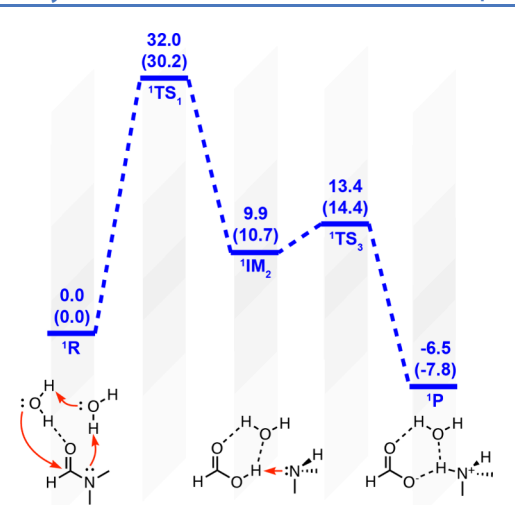


**Figure 2.** Reaction energy profile of the nonenzymatic hydrolysis of DMF calculated at the B3LYP/6-31G\* level of theory. Structures of the intermediates are shown with skeleton structures. Free energies and electronic energies (in parentheses) are shown above the energy profile, while labels for the intermediates and transition states are shown below the energy profile. Only intermediates with an adjacent transition state confirmed by vibrational analysis are shown. Intermediates and transition states are labeled with a superscript 1 (e.g., ¹R, ¹TS<sub>1</sub>, ¹IM<sub>2</sub>) to denote that the calculations were performed in the absence of an enzyme.

calculations align with experimental results showing that DMF is effectively inert in water unless a base such as hydroxide is present. 95,96

Having confirmed the high  ${}^{1}R^{-1}IM_{2}$  barrier of aqueous hydrolysis, we next investigated how the enzymatic reaction catalyzes the generation of the reactive hydroxide and how the enzyme positions proton donors and acceptors to facilitate the subsequent proton transfer required to trigger C–N bond cleavage. Experimental studies have suggested that multiple second-sphere residues are catalytically essential (His519, AsnS47, and Glu657) and could be capable of fulfilling these roles. Given that both His519 and Glu657 can catalyze the formation of the catalytic ferric hydroxide and facilitate proton

transfers, we explored both mechanisms, which we will refer to as the Glu657-initiated and His519-initiated mechanisms. In the crystal structure, the Glu657 carboxylate is 3.0 Å from the coordinating water, whereas the hydrogen bond acceptor nitrogen of His519 is 5.3 Å away (Supporting Information Figure S11). Classical MD simulations further show that Glu657 is consistently closer to DMF than His519, with an average distance to the DMF nitrogen of 6.0 and 7.4 Å, respectively, suggesting that Glu657 is better positioned to facilitate subsequent proton transfers (Supporting Information Figure S12). Moreover, previous molecular dynamics simulations found that a doubly protonated His519 forms a stable salt bridge with Glu657, which could hinder its ability to deprotonate water. We thus modeled His519 in the neutral N $\delta$ 1-protonated tautomer consistent with the H++-predicted protonation state (Supporting Information Table S1). The iron center was modeled as Fe(III) throughout the reaction, consistent with paramagnetic resonance data for native DMFase.<sup>13</sup> The possibility of redox activity involving more complex mechanisms or an exterior electron source was not modeled and remains a potential avenue for future study.

Thus, we first investigated the Glu657-initiated mechanism (Figure 3). In the reactant state of the Glu657-initiated mechanism (2R), water coordinates the iron metal site with two hydrogen bonds to Glu657. The reaction begins with a proton transfer from water to Glu657 (2TS1), generating the  $^{2}$ IM<sub>1</sub> hydroxide at  $\Delta G = 1.1$  kcal/mol relative to the reactant state (Figure 4 and Supporting Information Figure S13, Tables S7-S9). As the p $K_a$  of an average glutamate side chain is 4.5-5.0, it can be an effective base at pH 7 and can plausibly act as a proton acceptor. 97,98 To confirm the role of Glu657 as a proton acceptor, we calculated its  $pK_a$  to be 7.0 in the absence of DMF and 7.3 in its presence (Supporting Information Text S5 and Table S10). The calculated  $pK_a$  values are within the expected range necessary to deprotonate iron-bound water. The ferric hydroxide then hydroxylates the DMF carbonyl carbon ( ${}^{2}TS_{2}$ ) with a  $\Delta G^{\ddagger}$  value of 14.2 kcal/mol relative to the reactants, generating  ${}^{2}IM_{2}$  ( $\Delta G = 12.7$  kcal/mol). The protonated Glu657 then undergoes a conformational change to form a second hydrogen bond with the amine of the hydrated

**Figure 3.** Reaction schematic of the Glu657-initiated mechanism with skeleton structures depicting the following steps: (1) deprotonation of the coordinating water; (2) attack of the iron coordinating hydroxide at the carbonyl carbon of DMF; (3) conformational change of Glu657 to form a hydrogen bond with the amine of the hydrated DMF; (4) a proton transfer to the amine of the hydrated DMF; (5) deprotonation of the hydroxyl of the hydrated DMF; (6) cleavage of the C–N bond; (7) formation of a hydrogen bond between Asn547 and dimethylamine; (8) formation of a second hydrogen bond between dimethylamine and Glu657. Shorthand labels for each intermediate are indicated below the structures in blue.

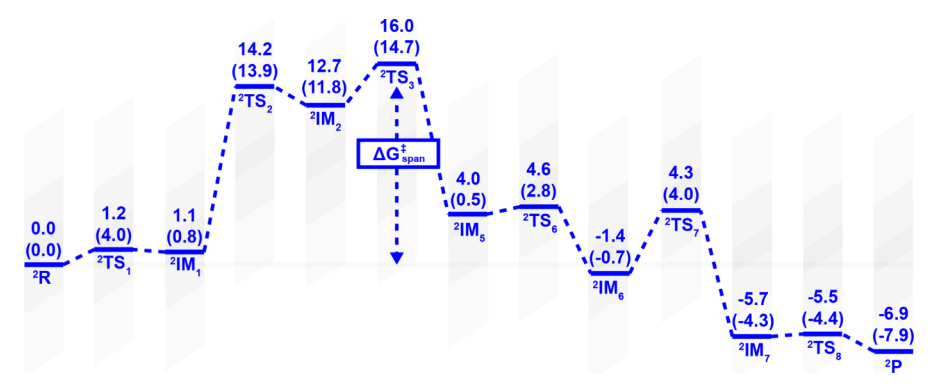


Figure 4. Reaction energy profile for the Glu657-initiated mechanism calculated at the B3LYP/LACVP\* level of theory. Free energies and electronic energies (in parentheses) are shown above the energy profile, while labels for the intermediates and transition states are below the energy profile. The energetic span  $(\Delta G^{\ddagger}_{span})$  is labeled on the free energy profile. Only intermediates with an adjacent transition state with a higher free energy are shown. Intermediates and transition states are labeled with a superscript 2 (e.g.,  ${}^2\mathbf{R}$ ,  ${}^2\mathbf{T}\mathbf{S}_1$ ,  ${}^2\mathbf{I}\mathbf{M}_2$ ) to denote that the calculations were performed for the Glu657-initiated mechanism.

DMF ( ${}^{2}$ IM<sub>3</sub>), corresponding to the rate-determining energetic span ( $\Delta G^{\ddagger}_{span}$  = 16.0 kcal/mol) relative to the reactants (Figure 4). This is followed by spontaneous proton transfers from Glu657 to the amine of DMF (2IM4) and then from the DMF hydroxyl to Glu657 to form  ${}^{2}$ IM<sub>5</sub> at  $\Delta G = 4.0$  kcal/mol (Figure 4). These proton transfers trigger C–N bond cleavage and the formation of dimethylamine and formate ( ${}^{2}IM_{6}$ ) with  $\Delta G = -1.4 \text{ kcal/mol}$  (Figure 4). The dimethylamine then dissociates to form a hydrogen bond with Asn547 (2IM<sub>7</sub>) at  $\Delta G = -5.7$  kcal/mol. Finally, the protonated Glu657 transfers a proton to dimethylamine to create the dimethylammonium product ( ${}^{2}\mathbf{P}$ ) at  $\Delta G = -6.9$  kcal/mol relative to the reactant state (Figure 4 and Supporting Information Movie 1). The energetic span of 16.0 kcal/mol was determined using the energetic span model with the reactant state (2R) as the turnover frequency (TOF)-determining transition state (Supporting Information Text S4). This span corresponds to a calculated TOF of 11.6 s<sup>-1</sup>, which is in agreement with the experimental turnover number  $(k_{\text{cat}} = 218 \text{ s}^{-1})^{13}$ , as they fall within the same order of magnitude. The experimental rate corresponds to an effective activation free energy of ~14.3 kcal/mol, a difference of only 1.7 kcal/mol, and within expected DFT error. Thus, the good agreement of the computational free energy barrier for the Glu657-initiated mechanism with the experimental activation free energy supports Glu657 as a potential base for generating the reactive hydroxide. 98 To validate the use of the sextet spin state for the mechanism, we also compared it to the intermediate-spin quartet and low-spin doublet states. The potential energy surface for this Glu657-initiated mechanism was calculated for all three spin states, confirming the sextet as the ground state across all intermediates and transition states (Supporting Information Figure S1). The sextet state was lower in energy than the quartet state by at least 11.7 kcal/mol and lower in energy than the doublet by at least 24.2 kcal/mol at every point along the reaction coordinate. Given this significant energetic separation, all subsequent enzymatic calculations were also performed using this lowest-energy sextet state.

We next investigated the reaction energetics for the alternative His519-initiated mechanism. In the reactant state (<sup>3</sup>R), the iron-coordinating water forms hydrogen bonds to His519 and Glu657 (Supporting Information Figure S14). If the water directly attacks the carbonyl carbon of DMF as in a previously proposed His519-initiated mechanism, <sup>13</sup> we obtain

a prohibitively high energetic barrier of  $\Delta G^{\ddagger}$  = 37.2 kcal/mol, effectively ruling this mechanism out as catalytically relevant (Supporting Information Figures S15 and S16). Thus, we investigated alternate reaction paths that generate a reactive hydroxide (Supporting Information Figures S14 and S17). In our proposed mechanism, the reaction is initiated with a proton transfer from the coordinating water to His519, generating the  ${}^{3}\text{IM}_{1}$  ferric hydroxide intermediate at  $\Delta G =$ 2.7 kcal/mol relative to the reactant state (3R) (Supporting Information Figure S18 and Tables S11-S13). Given that the  $pK_a$  of a histidine side chain is around 6.0, His519 is also expected to readily accept a proton from the coordinating water at pH 7.97,98 The protonated histidine then undergoes a conformational change to form a salt bridge with Glu657  $(^{3}IM_{2})$ . The hydroxide is then free to hydroxylate the carbonyl carbon of DMF with a  $\Delta G^{\ddagger}$  of 14.2 kcal/mol for  ${}^{3}TS_{3}$  relative to the reactants and forms  ${}^{3}\text{IM}_{3}$  at  $\Delta G = 11.2$  kcal/mol. The amine of DMF then undergoes pyramidal inversion (<sup>3</sup>IM<sub>4</sub>) together with the spontaneous formation of a His519-Asn547 hydrogen bond (<sup>3</sup>IM<sub>5</sub>). A proton is then transferred between Glu657 and hydroxylated DMF to form  ${}^{3}$ IM<sub>6</sub> at  $\Delta G = 13.2$ kcal/mol. Glu657 then undergoes a conformational change and transfers the proton to the DMF amine with a  $\Delta G^{\ddagger}_{\text{span}}$  of 22.9 kcal/mol corresponding to the rate-determining energetic span, forming  ${}^{3}IM_{7}$  at  $\Delta G = 10.7$  kcal/mol (Supporting Information Figure S18). In the His519-initiated mechanism, this conformational change is less favorable, with a ratedetermining energetic span of 22.9 kcal/mol compared to 16.0 kcal/mol in the Glu657-initiated pathway, likely due to restricted Glu657 mobility caused by its proximity to the protonated His519. Next, protonation of the DMF amine triggers C-N bond cleavage to form  ${}^3\text{IM}_8$  at a  $\Delta G$  of 9.4 kcal/ mol. Finally, hydrogen bonds form between dimethylamine and Glu657 and Asn547 to generate the product state (3P) at a  $\Delta G$  of 5.2 kcal/mol. Both the Glu657-initiated and His519initiated mechanisms exhibit significantly lower barriers than the nonenzymatic reaction (Supporting Information Movie 2). While our results indicate that both Glu657 and His519 can generate the reactive hydroxide, the Glu657-initiated pathway proceeds with a lower overall energetic span (16.0 kcal/mol) compared with the His519-initiated mechanism (22.9 kcal/ mol), which has a calculated TOF of  $1.02 \times 10^{-4}$  s<sup>-1</sup>.

**3.2. Mechanistic Roles of Second-Sphere Residues.** While experimental mutagenesis has indicated that residues in

the second coordination sphere of DMFase are essential for catalysis, 13 the mechanism by which these residues influence the reaction remains unknown. We included His519, Tyr522, Asn547, and Glu657 in our QM cluster models based on the CSA method<sup>66,67</sup> and previous experimental mutagenesis studies of Asn547 and His519 (Supporting Information Text S3 and Figure S6). 13 We also included Lys567 as it is highly conserved across similar enzymes and likely forms a cation- $\pi$ interaction with coordinating Tyr440.<sup>99</sup> Although Lys567 was below our CSA threshold, it exhibited the sixth-highest positive charge shift and would likely be identified using a complementary method such as Fukui shift analysis (FSA), which evaluates how specific residues perturb the frontier molecular orbitals.<sup>66</sup> Although we did not perform further analysis for Tyr522, its inclusion was necessary to preserve the native conformation of Lys567 and support the structural context of the cation- $\pi$  interaction. Among the coordination sphere residues His519, Asn547, Lys567, and Glu657, we first focused on Glu657 as our reaction path analysis identified it as essential for initiating the reaction. To further investigate the role of Glu657 in the reaction, we quantified the strength of the hydrogen bonding interactions using QTAIM (Section 2). In the reactant state (2R), the strongest hydrogen bond was observed between Glu657 and the coordinating water, while in the hydroxide-bound state ( ${}^{2}IM_{1}$ ), the strongest hydrogen bond is between protonated (i.e., neutral) Glu657 and the ferric hydroxide. The stabilization was −26.5 kcal/mol in <sup>2</sup>R and -16.5 kcal/mol in <sup>2</sup>IM<sub>1</sub> (Figure 5 and Supporting Information Figure S19). While estimating hydrogen bond strength from the electron density is known to overestimate the interaction energy, <sup>100</sup> these high hydrogen bond strengths for charge-assisted hydrogen bonds indicate that the orientation of Glu657 observed in the crystal structure

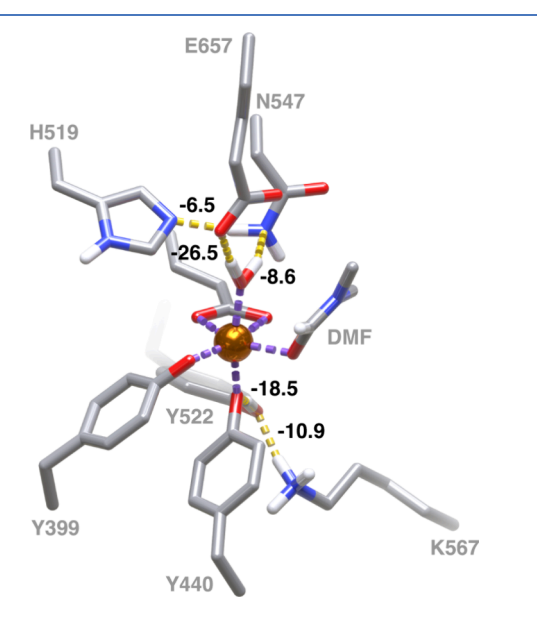


Figure 5. Quantification of the hydrogen bond strengths (kcal/mol) in the reactant state  $(^2R)$  of the Glu657-initiated mechanism using QTAIM. Hydrogen bond strengths are labeled in black in kcal/mol, and amino acids are labeled in gray. Atoms are colored as follows: carbon in gray, nitrogen in blue, oxygen in red, hydrogen in white, and iron in dark orange. Coordinating bonds are shown as purple dashed lines and hydrogen bonds are shown in yellow dashed lines. Backbone atoms and hydrogens are omitted for clarity except where necessary to illustrate protonation states.

corresponds to a strong interaction with water and that Glu657 is positioned to generate the ferric hydroxide (Figure 5).

We next investigated the roles of His519 and Asn547, which are not directly involved in the most likely Glu657-initiated reaction mechanism but form noncovalent interactions with the active site. While the noncovalent interactions of Glu657 are predominantly strong hydrogen bonds to the metal-bound water, His519 and Asn547 maintain a single hydrogen bond with each other throughout the reaction cycle, with a stabilization computed to be -6.5 kcal/mol in  ${}^{2}R$  (Figure 5). To gain a more complete understanding of the energetic contributions of His519 and Asn547 beyond hydrogen bonding, we quantified the energetic contribution for each residue across the reaction pathway using ALMO-EDA (Section 2). ALMO-EDA shows that His519 provides favorable energetic stabilization along the reaction pathway as its associated Pauli-repulsion term generally decreases from one intermediate or transition state to the next (Figure 6). To further explore the role of His519, we visualized the complementary occupied-virtual pairs (COVP), which identify the His519-Asn547 hydrogen bond as the dominant interaction with an energy of -9.9 kcal/mol (Figure 6). We performed similar analyses for Asn547 and found that Asn547 stabilizes the highest-energy transition state (2TS<sub>3</sub>) in two ways. The Pauli-repulsion term is lower in this TS than in the immediately preceding intermediate (2IM2), and its electrostatic, dispersion, and charge transfer contributions are more favorable than those in <sup>2</sup>IM<sub>1</sub>, the point where the energy profile begins to climb toward the highest-energy point (<sup>2</sup>TS<sub>3</sub>, Supporting Information Figure S20). We also observed favorable repulsion energetics, stabilizing <sup>2</sup>TS<sub>3</sub> relative to <sup>2</sup>IM<sub>2</sub>.

While His519 and Asn547 contribute to transition state stabilization, we also investigated the conserved residue, Lys567, which forms a cation- $\pi$  interaction with residue Tyr440, <sup>101</sup> to assess whether it similarly modulates reactivity. To investigate the potential cation- $\pi$  interaction, we first calculated the energy difference between the Lys567-Tyr440 complex and the sum of the isolated Lys567 and Tyr440 fragments. This computed interaction energy of -16.3 kcal/ mol is consistent with a moderately strong cation- $\pi$ interaction (Supporting Information Figure S21). To quantify the specific energetic contributions of this interaction along the catalytic pathway and its effect on reactivity, we performed an ALMO-EDA analysis of Lys567 across all intermediates and transition states, as this method enables decomposition of residue-specific energetic contributions, unlike local electron density-based approaches such as QTAIM. Although we did not observe a significant decrease in the rate-determining transition state from any single energy component, the electrostatic term was the most stabilizing across the entire reaction path, ranging from -17.5 to -19.5 kcal/mol, consistent with expectations for an electrostatic driving force for cation- $\pi$  interactions (Supporting Information Figure S22). These results suggest that the conserved Lys567 residue and its cation- $\pi$  interaction with Tyr440 modulate the active site electrostatics similarly across all steps.

Given the importance of the tyrosinate state of the coordinating Tyr399 and Tyr440 residues in binding iron, we investigated whether the cation— $\pi$  interaction could stabilize the anionic state. To isolate the effect of the cation— $\pi$  interaction on Tyr440 deprotonation, we constructed a smaller QM cluster model without iron containing Tyr440, Glu521,

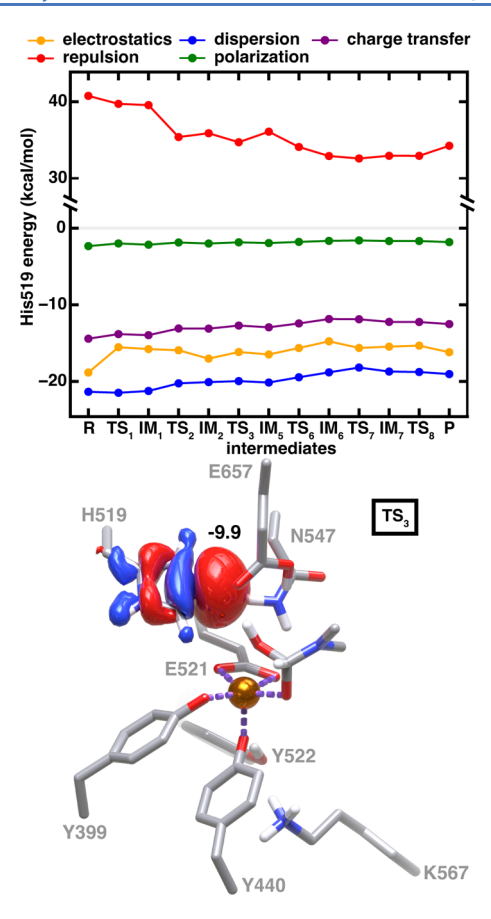


Figure 6. ALMO-EDA energy-decomposition components for His519 for the Glu657-catalyzed reaction. (top) Energy decomposition for all intermediates and transition states broken into electrostatics (orange), dispersion (blue), charge transfer (purple), repulsion (red), and polarization (green). (bottom) Visualization of the complementary occupied-virtual pairs (COVP) for the stabilizing interaction between His519 and the rest of the QM cluster model. The isosurface values were set to +0.03 (blue) and -0.03 (red) for the COVPs. The energetic strength of the depicted COVP is labeled in kcal/mol. Residues are labeled in gray. Atoms are colored as follows: carbon in gray, nitrogen in blue, oxygen in red, hydrogen in white, and iron in dark orange. Coordinating bonds are shown as purple dashed lines. Backbone atoms and hydrogens are omitted for clarity except where necessary to illustrate protonation states.

Lys567, and Tyr522, with the latter included to preserve the native conformation of Lys567 given our previous results showing that Tyr522 forms strong hydrogen bonds with both Tyr440 and Lys567 with strengths of -18.5 and -10.9 kcal/ mol, respectively (Figure 5). When the cation  $-\pi$  interaction was included, we found that the deprotonation of Tyr440 by Glu521 was practically barrierless ( $\Delta E^{\ddagger} = 0.2 \text{ kcal/mol}$ ) and the anionic state to be -4.5 kcal/mol more stable than the neutral tyrosine (Supporting Information Figure S23). However, when Lys567 was not included, we found the tyrosinate to be 7.8 kcal/mol less stable than the reactants with no local minimum on the electronic energy surface (Supporting Information Figure S24). To confirm this key stabilizing role in a more complete model, we repeated the deprotonation calculations using the full QM cluster active site, omitting the iron center to represent the precoordination state. These calculations are in good agreement with our findings from the minimal model, as the deprotonation of Tyr440 remains barrierless with Lys567 present but becomes energetically unfavorable with an electronic energy barrier of 3.9 kcal/mol in its absence (Supporting Information Figure S25 and S26). Motivated by this finding, we also investigated whether the nearby Trp473 plays a similar role in stabilizing the deprotonation of equatorial Tyr399 through the interaction of the Trp473 pyrrole-NH with the  $\pi$ -system of Tyr399. In contrast to the Lys567–Tyr440 interaction, Trp473 provides only a modest stabilization to the deprotonation of Tyr399 by Glu657, lowering the barrier by just 0.6 kcal/mol from 7.4 to 6.8 kcal/mol (Supporting Information Figures S27 and S28). This minor effect, when compared to the critical role of Lys567, suggests that Trp473 is not essential for promoting the tyrosinate state of Tyr399 but rather contributes to the general stability of the active site architecture.

Given that the cation  $-\pi$  interaction stabilizes the negative charge on Tyr440, we investigated whether this could influence the coordinating Fe(III)-Tyr440 bond length by calculating the bond lengths for all of the coordinating bonds over the course of the full reaction. We observed that the Fe(III)-Tyr440 bond length was moderately shorter than the Fe(III)— Tyr399 bond length across the entirety of the mechanism, with average bond lengths of 1.88 and 1.95 Å, respectively (Supporting Information Figure S29). To better understand this difference in bond length, we performed geometry optimizations on all intermediates with Lys567 removed from the model. Upon removal of Lys567, the Fe(III)-Tyr440 bond length shortened across all intermediates in the catalytic cycle, with an average bond length of 1.92 Å (Supporting Information Figure S30). While these calculations confirm that the cation  $-\pi$  interaction with Lys567 elongates the Fe(III)-Tyr440 bond, the axial Tyr440 bond remains 0.03 Å longer on average than the equatorial Tyr399 bond in the absence of Lys567. These findings suggest that the observed difference in the Fe-tyrosinate bond lengths arises from a combination of the stabilizing cation– $\pi$  interaction and a trans effect inherent to the axial coordination position.

Together, these results highlight distinct roles for second coordination sphere residues in DMFase catalysis. Glu657 directly facilitates the reaction by acting as a proton acceptor and donor through a series of hydrogen bonding interactions with the metal-bound water and DMF. In contrast, His519 and Asn547 contribute indirectly by stabilizing the highest-energy transition state and modulating repulsive interactions along the reaction pathway. Meanwhile, Lys567 plays a structural role by stabilizing the anionic form of Tyr440 through the cation— $\pi$  interaction structurally mediated by Tyr522, thereby promoting the initial Fe(III) coordination. Based on these findings, we propose Glu657 and Lys567 as targets for mutagenesis to confirm their mechanistic roles in DMFase catalysis.

**3.3.** Role of the 2Tyr-1Glu Motif in Reactivity. To determine whether the unusual 2Tyr-1Glu motif provides catalytic advantages over the more common 2His-1Glu system, we substituted Tyr399 and Tyr440 with histidines and evaluated the resulting reactivity. To directly compare these coordination environments, we examined the first five steps of the Glu657-initiated pathway, which include the highest-energy transition state. Specifically, we compared the native Fe(III)-2Tyr-1Glu active site to two histidine-substituted variants: an Fe(II)-2His-1Glu system representing the more common NHIE oxidation state and an Fe(III)-2His-1Glu system to isolate the effect of oxidation state on reactivity (Supporting Information Table S1 and Figure S2). Given that the oxidation state of iron in the mutant 2His-1Glu-

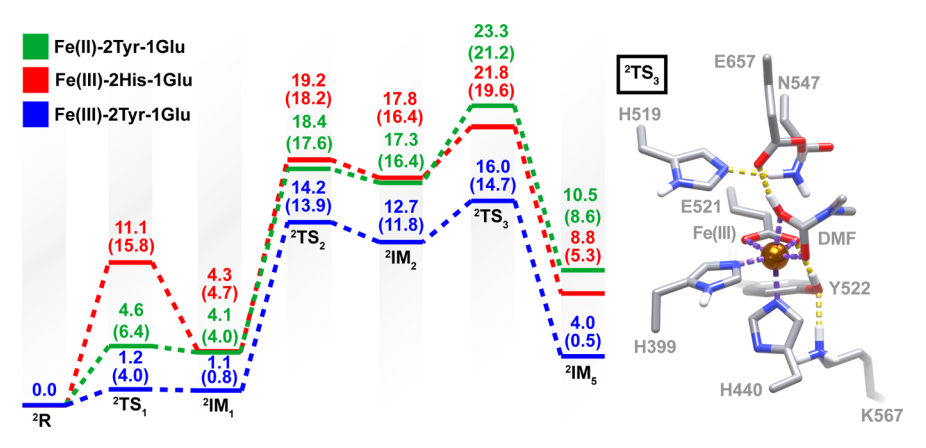


Figure 7. (left) Reaction energy diagram of the Glu657-initiated mechanism comparing the Fe(II)-2His-1Glu active site (green), the Fe(III)-2His-1Glu active site (red), and the native Fe(III)-2Tyr-1Glu active site (blue), including the rate-determining step. Energies were calculated at the B3LYP/LACVP\* level of theory. Energies are reported in kcal/mol above each intermediate or transition state, with free energies ( $\Delta G$ ) indicated above and electronic energies ( $\Delta E$ ) indicated below in parentheses. Intermediates and transition states are labeled with a superscript 2 (e.g.,  $^2$ R,  $^2$ TS<sub>1</sub>,  $^2$ IM<sub>2</sub>) to denote that the calculations were performed for the Glu657-initiated mechanism. (right) Geometry of the highest-energy transition state for the Fe(III)-2His-1Glu active site, with residues labeled in gray. Atoms are colored as follows: carbon in gray, nitrogen in blue, oxygen in red, hydrogen in white, and iron in dark orange. Coordinating bonds are shown as purple dashed lines, and hydrogen bonds are shown as yellow dashed lines. Amino acids are labeled in gray. Backbone atoms and hydrogens are omitted for clarity except where necessary to illustrate protonation states.

coordinated DMFase has not been established experimentally, unlike the Fe(III)-2Tyr-1Glu system, we examined both Fe(II) and Fe(III) to isolate the effect of oxidation state from coordinating residue identity. For the reaction calculated using the Fe(II) 2His-1Glu system, the highest-energy transition state ( ${}^{2}TS_{3}$ ) has a  $\Delta E^{\ddagger}$  of 22.3 kcal/mol relative to the reactants (Supporting Information Figure S31). Full characterization of the transition states reveals a rate-determining energetic span of  $\Delta G^{\ddagger}$  of 23.3 kcal/mol for  ${}^{2}TS_{3}$  relative to the reactants (Figure 7 and Supporting Information Tables S14 and S15). Thus, replacing Tyr399 and Tyr440 with histidine residues in the presence of the more common Fe(II) yields a rate-determining energetic span ( $\Delta G^{\ddagger}_{span} = 23.3 \text{ kcal/mol}$ ) that is lower than the nonenzymatic case (32.0 kcal/mol) but 7.3 kcal/mol higher than the native Fe(III)-2Tyr-1Glu active site  $(\Delta G_{\text{span}}^{\ddagger} = 16.0 \text{ kcal/mol})$ . The energetic penalty introduced by histidine substitution is approximately uniform across all steps beyond the reactant, consistent with the overstabilization of the reactant state relative to the rate-determining transition state.

To decouple the effect of oxidation state from ligand identity, we investigated how a 2His-1Glu active site influences reaction energetics when the iron oxidation state is +3, as observed natively in DMFase. The <sup>2</sup>TS<sub>3</sub> transition state identified by NEB calculations has a  $\Delta E^{\ddagger}$  of 19.7 kcal/mol relative to the reactants (Supporting Information Figure S32). After transition state characterization, the highest-energy transition state ( ${}^{2}TS_{3}$ ) has a  $\Delta G^{\ddagger}$  of 21.8 kcal/mol, corresponding to the energetic span (Figure 7 and Supporting Information Tables S16 and S17). These results show that the Fe(III)-2Tyr-1Glu motif provides free energy stabilization of the rate-determining transition state by 5.8 kcal/mol compared to the Fe(III)-2His-1Glu motif, even when the oxidation state is consistent. The higher observed barrier for the Fe(III)-2His-1Glu motif results from both overstabilization of the reactant state relative to the intermediate <sup>2</sup>IM<sub>1</sub> and destabilization of the highest-energy transition state <sup>2</sup>TS<sub>3</sub> relative to the reactant. We observe that the  $\Delta G^{\ddagger}$  of  ${}^{2}TS_{3}$  relative to  ${}^{2}IM_{1}$  is moderately higher for the Fe(III)-2His-1Glu (17.5 kcal/mol)

motif compared to the Fe(III)-2Tyr-1Glu (14.9 kcal/mol) motif and this 2.6 kcal/mol increase is nearly matched by a 3.2 kcal/mol stabilization of the Fe(III)-2His-1Glu reactant state relative to <sup>2</sup>IM<sub>1</sub> (Figure 7). Although these results confirm that the native Fe(III)-2Tyr-1Glu motif yields more favorable energetics compared to the 2His-1Glu motif irrespective of the iron oxidation state, the barrier reduction observed upon increasing the iron oxidation state from Fe(II) to Fe(III) ( $\Delta G^{\ddagger}$ reduced from 23.3 to 21.8 kcal/mol) underscores the potential importance of enhancing the Lewis acidity of the metal center. These differences in energetic span correspond to a significant variation in catalytic efficiency, as quantified by the calculated TOF. The native Fe(III)-2Tyr-1Glu active site has a calculated TOF of 11.6 s<sup>-1</sup>, whereas the Fe(III)-2His-1Glu and Fe(II)-2His-1Glu variants are markedly slower, with calculated TOFs of  $5.9 \times 10^{-4}$  and  $5.6 \times 10^{-5}$  s<sup>-1</sup>, respectively (Supporting Information Text S4). Given the more favorable energetics of the 2Tyr-1Glu motif and the decrease in barrier height with an increasing oxidation state, we investigated whether introducing electron-withdrawing fluorine substituents at the 3 and 5 positions of the Tyr rings could further enhance the Lewis acidity of the iron center. Using a fluorinated QM active site model, the highest-energy transition state has a  $\Delta E^{\ddagger}$  of 13.8 kcal/mol relative to the reactants (Supporting Information Figure S33). Characterization of the transition states resulted in a  $\Delta G$  of 15.5 kcal/mol for the highest-energy transition state, <sup>2</sup>TS<sub>3</sub> (Supporting Information Figure S34 and Tables S18, S19). The free energy stabilization of the rate-determining transition state by only 0.5 kcal/mol relative to the unmodified system suggests that the choice of the native tyrosines is finely tuned for the hydrolysis of DMF. Together, these comparisons show that coordination by tyrosine results in a more favorable active site than histidine, as it avoids reactant overstabilization and lowers the relative barrier. The advantage stems from shaping the entire energy landscape, not merely lowering a single barrier, and further electronic tuning by fluorination offers little additional benefit. However, while we cannot exclude contributions from protein dynamics or distal residues, these results demonstrate how the crystallographic pose and

ACS Catalysis pubs.acs.org/acscatalysis Research Article

experimentally validated residues can rationalize the 2Tyr-1Glu motif and highlight its finely tuned electrostatic match to the hydrolytic chemistry of DMFase.

#### 4. CONCLUSIONS

We performed extensive computational investigations of the catalytic mechanism of N,N-dimethylformamidase (DMFase), a nonheme iron enzyme featuring an atypical Fe(III)-2Tyr-1Glu coordination motif that enables hydrolytic activity toward the environmental contaminant DMF. We identified two distinct mechanistic pathways for hydroxide formation in DMFase, initiated by second coordination sphere residues Glu657 and His519, through large quantum mechanical cluster models, charge shift analysis, energy decomposition, and coordination and hydrogen bonding analysis. Both Glu657 and His519 enable the formation of a reactive ferric hydroxide, but the Glu657-initiated mechanism is energetically preferred with both activation barriers and more favorable reaction thermodynamics. We found that the second coordination sphere residues play distinct roles: Glu657 mediates proton transfers through strong hydrogen bonding; His519 and Asn547 stabilize the highest-energy transition state via favorable noncovalent interactions; and Lys567 stabilizes the deprotonated tyrosinate state of Tyr440 through a cation- $\pi$ interaction, a prerequisite for iron coordination and formation of the functional active site. Future work could also consider alternative protonation states, such as a doubly protonated His519 acting in a manner similar to Lys567.

We next aimed to elucidate the potential role that this nonstandard 2Tyr-1Glu active site played in catalysis. Substituting the native tyrosinate ligands with more common active site histidines destabilized the reaction pathway, even when the Fe(III) oxidation state was preserved, underscoring the functional importance of the coordination of Fe by tyrosinate residues. This electronic tuning arises from the combined effects of Fe(III), which enhances Lewis acidity, and coordination of Fe by tyrosinate residues, which selectively stabilizes key transition states and intermediates. These findings demonstrate how the 2Tyr-1Glu primary coordination sphere enables hydrolytic reactivity in a nonheme iron enzyme lacking coordinating histidines. The combination of this coordination motif with catalytically positioned second-sphere residues such as Glu657 may offer a strategy for introducing hydrolytic activity into otherwise oxidative nonheme iron scaffolds. Given the general simplicity of the hydrolysis mechanism, engineering the binding pocket to accommodate other substrates bearing amide bonds may enable broader applications in bioremediation. Contaminants with similar electrophilic amide moieties may be viable targets for future substrate profiling or directed evolution. Further investigation of the coordinating residues, such as the impact of bond length or angle distortions on hydroxide activation or substrate coordination, could offer insights into how tuning the active site geometry modulates hydrolytic activity. Such studies may also aid in the design of biomimetic or synthetic scaffolds with a tailored reactivity.

# ASSOCIATED CONTENT

### **Data Availability Statement**

A Zenodo repository containing supporting Python scripts and topology files for MD and QM/MM input is available at 10. 5281/zenodo.15427850.

# **Solution** Supporting Information

The Supporting Information is available free of charge at https://pubs.acs.org/doi/10.1021/acscatal.5c03335.

Movie 1 depicting the full QM-optimized NEB reaction path for the Glu657-initiated hydrolysis mechanism of DMFase (ZIP)

Movie 2 depicting the full QM-optimized NEB reaction path for the His519-initiated hydrolysis mechanism of DMFase (ZIP)

System preparation and protonation states for classical MD; MCPB-derived iron parameters and atom labels; trajectory clustering statistics and representative structure selection; QM/MM setup and charge shift analysis details; summary of QM cluster models including fluorinated and histidine variants; LOBA oxidation state analysis for catalytic intermediates; nonenzymatic hydrolysis water network, energetics, and structures; NEB reaction profiles and energetics for Glu657 and His519-initiated mechanisms; basis set sensitivity and imaginary frequency validation; energy profiles for direct attack and cation— $\pi$  interaction variants; QTAIM hydrogen bond energies and ALMO-EDA decomposition for key residues; comparison of Fe(II)/Fe(III) and 2His-1Glu/fluorotyrosine models.  $^{101}$  (PDF)

#### AUTHOR INFORMATION

# **Corresponding Author**

Heather J. Kulik – Department of Chemical Engineering and Department of Chemistry, Massachusetts Institute of Technology, Cambridge, Massachusetts 02139, United States; orcid.org/0000-0001-9342-0191; Email: hjkulik@mit.edu

# **Authors**

David W. Kastner — Department of Chemical Engineering and Department of Biological Engineering, Massachusetts Institute of Technology, Cambridge, Massachusetts 02139, United States; orcid.org/0000-0002-7766-4249

Clorice R. Reinhardt — Department of Chemical Engineering, Massachusetts Institute of Technology, Cambridge, Massachusetts 02139, United States; orcid.org/0000-0002-6083-4950

Husain Adamji – Department of Chemical Engineering, Massachusetts Institute of Technology, Cambridge, Massachusetts 02139, United States; ○ orcid.org/0000-0003-3058-680X

Terence S. Oscar-Okpala – Department of Chemical Engineering, Massachusetts Institute of Technology, Cambridge, Massachusetts 02139, United States

Ilia Kevlishvili — Department of Chemical Engineering, Massachusetts Institute of Technology, Cambridge, Massachusetts 02139, United States; orcid.org/0000-0001-8133-4165

Yuriy Román-Leshkov — Department of Chemical Engineering and Department of Chemistry, Massachusetts Institute of Technology, Cambridge, Massachusetts 02139, United States; orcid.org/0000-0002-0025-4233

Complete contact information is available at: https://pubs.acs.org/10.1021/acscatal.5c03335

#### Notes

The authors declare no competing financial interest.

#### ACKNOWLEDGMENTS

This work was primarily supported by the National Institute of General Medical Sciences of the National Institutes of Health under award number R35GM152027 (to H.J.K. and D.W.K.). Initial support was provided by the U.S. Department of Energy, Office of Science, Office of Advanced Scientific Computing, Office of Basic Energy Sciences, via the Scientific Discovery through Advanced Computing (SciDAC) program (to D.W.K., C.R., and H.J.K.) as well as by the National Science Foundation under grant number CBET-1846426 (to H.A. and H.J.K.). Partial support was provided by the National Science Foundation Graduate Research Fellowships under Grant #1745302 for D.W.K., an Arnold O. Beckman Postdoctoral fellowship for C.R., and a fellowship from the MIT Energy Initiative, supported by Shell, for H.A. Y.R.-L. acknowledges support from the US Department of Energy, Office of Basic Energy Sciences, under award no. DE-SC0016214. The authors thank Adam H. Steeves for providing a critical reading of the manuscript.

# REFERENCES

- (1) Müller, R.-J.; Schrader, H.; Profe, J.; Dresler, K.; Deckwer, W.-D. Enzymatic Degradation of Poly(Ethylene Terephthalate): Rapid Hydrolyse Using a Hydrolase from T. Fusca. Macromol. Rapid Commun. 2005, 26, 1400–1405.
- (2) Silva, C. M.; Carneiro, F.; O'Neill, A.; Fonseca, L. P.; Cabral, J. S. M.; Guebitz, G.; Cavaco-Paulo, A. Cutinase—a New Tool for Biomodification of Synthetic Fibers. *J. Polym. Sci., Part A:Polym. Chem.* **2005**, 43, 2448–2450.
- (3) Roth, C.; Wei, R.; Oeser, T.; Then, J.; Föllner, C.; Zimmermann, W.; Sträter, N. Structural and Functional Studies on a Thermostable Polyethylene Terephthalate Degrading Hydrolase from Thermobifida Fusca. *Appl. Microbiol. Biotechnol.* **2014**, *98*, 7815–7823.
- (4) Yoshida, S.; Hiraga, K.; Takehana, T.; Taniguchi, I.; Yamaji, H.; Maeda, Y.; Toyohara, K.; Miyamoto, K.; Kimura, Y.; Oda, K. A Bacterium That Degrades and Assimilates Poly(Ethylene Terephthalate). *Science* **2016**, *351*, 1196–1199.
- (5) Zrimec, J.; Kokina, M.; Jonasson, S.; Zorrilla, F.; Zelezniak, A. Plastic-Degrading Potential across the Global Microbiome Correlates with Recent Pollution Trends. *mBio* **2021**, *12*, No. e02155-21.
- (6) Zhang, S.-T.; Deng, S.-K.; Li, T.; Maloney, M. E.; Li, D.-F.; Spain, J. C.; Zhou, N.-Y. Discovery of the 1-Naphthylamine Biodegradation Pathway Reveals a Broad-Substrate-Spectrum Enzyme Catalyzing 1-Naphthylamine Glutamylation. *eLife* **2024**, *13*, No. e95555.
- (7) Ghisalba, O.; Cevey, P.; Küenzi, M.; Schär, H.-P. Biodegradation of Chemical Waste by Specialized Methylotrophs, an Alternative to Physical Methods of Waste Disposal. *Conserv. Recycl.* **1985**, *8*, 47–71.
- (8) Urakami, T.; Kobayashi, H.; Araki, H. Isolation and Identification of N,N-Dimethylformamide-Biodegrading Bacteria. *J. Ferment. Bioeng.* **1990**, *70*, 45–47.
- (9) Rylott, E. L.; Jackson, R. G.; Sabbadin, F.; Seth-Smith, H. M. B.; Edwards, J.; Chong, C. S.; Strand, S. E.; Grogan, G.; Bruce, N. C. The Explosive-Degrading Cytochrome P450 XplA: Biochemistry, Structural Features and Prospects for Bioremediation. *Biochim. Biophys. Acta, Proteins Proteomics* **2011**, *1814*, 230–236.
- (10) Ren, Y.; Manefield, M. Evolution of Pollutant Biodegradation. *Appl. Microbiol. Biotechnol.* **2025**, *109*, 36.
- (11) Schär, H.-P.; Holzmann, W.; Ramos Tombo, G. M.; Ghisalba, O. Purification and Characterization of N,N-dimethylformamidase from Pseudomonas DMF 3/3. *Eur. J. Biochem.* **1986**, *158*, 469–475.
- (12) Hasegawa, Y.; Matsuo, M.; Sigemoto, Y.; Sakai, T.; Tokuyama, T. Purification and Characterization of N,N-dimethylformamidase from Alcaligenes Sp. KUFA-1. *J. Ferment. Bioeng.* **1997**, *84*, 543–547.
- (13) Arya, C. K.; Yadav, S.; Fine, J.; Casanal, A.; Chopra, G.; Ramanathan, G.; Vinothkumar, K. R.; Subramanian, R. A 2-Tyr-1-

- Carboxylate Mononuclear Iron Center Forms the Active Site of a Paracoccus Dimethylformamidase. *Angew. Chem., Int. Ed. Engl.* **2020**, 59, 16961–16966.
- (14) Koehntop, K. D.; Emerson, J. P.; Que, L., Jr. The 2-His-1-Carboxylate Facial Triad: A Versatile Platform for Dioxygen Activation by Mononuclear Non-Heme Iron(II) Enzymes. *JBIC*, *J. Biol. Inorg. Chem.* **2005**, *10*, 87–93.
- (15) Borowski, T.; Bassan, A.; Siegbahn, P. E. M. Mechanism of Dioxygen Activation in 2-Oxoglutarate-Dependent Enzymes: A Hybrid Dft Study. *Chem. Eur. J.* **2004**, *10*, 1031–1041.
- (16) Dai, Y.; Li, N.; Zhao, Q.; Xie, S. Bioremediation Using Novosphingobium Strain Dy4 for 2,4-Dichlorophenoxyacetic Acid-Contaminated Soil and Impact on Microbial Community Structure. *Biodegradation* **2015**, *26*, 161–170.
- (17) Bopp, C. E.; Bernet, N. M.; Kohler, H.-P. E.; Hofstetter, T. B. Elucidating the Role of O2 Uncoupling in the Oxidative Biodegradation of Organic Contaminants by Rieske Non-Heme Iron Dioxygenases. *ACS Environ. Au* **2022**, *2*, 428–440.
- (18) Duarte, M.; Nielsen, A.; Camarinha-Silva, A.; Vilchez-Vargas, R.; Bruls, T.; Wos-Oxley, M. L.; Jauregui, R.; Pieper, D. H. Functional Soil Metagenomics: Elucidation of Polycyclic Aromatic Hydrocarbon Degradation Potential Following 12 Years of in Situ Bioremediation. *Environ. Microbiol.* **2017**, *19*, 2992–3011.
- (19) Kauppi, B.; Lee, K.; Carredano, E.; Parales, R. E.; Gibson, D. T.; Eklund, H.; Ramaswamy, S. Structure of an Aromatic-Ring-Hydroxylating Dioxygenase—Naphthalene 1,2-Dioxygenase. *Structure* 1998, 6, 571–586.
- (20) Barry, S. M.; Challis, G. L. Mechanism and Catalytic Diversity of Rieske Non-Heme Iron-Dependent Oxygenases. *ACS Catal.* **2013**, 3, 2362–2370.
- (21) Brennerova, M. V.; Josefiova, J.; Brenner, V.; Pieper, D. H.; Junca, H. Metagenomics Reveals Diversity and Abundance of Meta-Cleavage Pathways in Microbial Communities from Soil Highly Contaminated with Jet Fuel under Air-Sparging Bioremediation. *Environ. Microbiol.* **2009**, *11*, 2216–2227.
- (22) Price, J. C.; Barr, E. W.; Tirupati, B.; Bollinger, J. M.; Krebs, C. The First Direct Characterization of a High-Valent Iron Intermediate in the Reaction of an A-Ketoglutarate-Dependent Dioxygenase: A High-Spin Fe(IV) Complex in Taurine/A-Ketoglutarate Dioxygenase (TauD) from Escherichia Coli. *Biochemistry* **2003**, *42*, 7497–7508.
- (23) Price, J. C.; Barr, E. W.; Glass, T. E.; Krebs, C.; Bollinger, J. M. Evidence for Hydrogen Abstraction from C1 of Taurine by the High-Spin Fe(IV) Intermediate Detected During Oxygen Activation by Taurine:A-Ketoglutarate Dioxygenase (TauD). *J. Am. Chem. Soc.* **2003**, *125*, 13008–13009.
- (24) Chakrabarty, S.; Wang, Y.; Perkins, J. C.; Narayan, A. R. H. Scalable Biocatalytic C—H Oxyfunctionalization Reactions. *Chem. Soc. Rev.* **2020**, *49*, 8137—8155.
- (25) Liu, J.; Tian, J.; Perry, C.; Lukowski, A. L.; Doukov, T. I.; Narayan, A. R. H.; Bridwell-Rabb, J. Design Principles for Site-Selective Hydroxylation by a Rieske Oxygenase. *Nat. Commun.* **2022**, *13*, 255.
- (26) Vaillancourt, F. H.; Yin, J.; Walsh, C. T. SyrB2 in Syringomycin E Biosynthesis Is a Nonheme FeII-Ketoglutarate- and O2-Dependent halogenase. *Proc. Natl. Acad. Sci. U. S. A.* **2005**, *102*, 10111–10116.
- (27) Mitchell, A. J.; Zhu, Q.; Maggiolo, A. O.; Ananth, N. R.; Hillwig, M. L.; Liu, X.; Boal, A. K. Structural Basis for Halogenation by Iron- and 2-Oxo-Glutarate-Dependent Enzyme Welo5. *Nat. Chem. Biol.* **2016**, *12*, 636–640.
- (28) Martinez, S.; Hausinger, R. P. Catalytic Mechanisms of Fe(II)-and 2-Oxoglutarate-Dependent Oxygenases. *J. Biol. Chem.* **2015**, 290, 20702–20711.
- (29) Del Rio Flores, A.; Zhai, R.; Kastner, D. W.; Seshadri, K.; Yang, S.; De Matias, K.; Shen, Y.; Cai, W.; Narayanamoorthy, M.; Do, N. B.; Xue, Z.; Marzooqi, D. A.; Kulik, H. J.; Zhang, W. Enzymatic Synthesis of Azide by a Promiscuous N-Nitrosylase. *Nat. Chem.* **2024**, *16*, 2066–2075.
- (30) Del Rio Flores, A.; Kastner, D. W.; Du, Y.; Narayanamoorthy, M.; Shen, Y.; Cai, W.; Vennelakanti, V.; Zill, N. A.; Dell, L. B.; Zhai,

- R.; Kulik, H. J.; Zhang, W. Probing the Mechanism of Isonitrile Formation by a Non-Heme Iron(II)-Dependent Oxidase/Decarboxylase. *J. Am. Chem. Soc.* **2022**, *144*, 5893. 10.1021/jacs.1c12891
- (31) Jonnalagadda, R.; Flores, A. D.; Cai, W. L.; Mehmood, R.; Narayanamoorthy, M.; Ren, C. X.; Zaragoza, J. P. T.; Kulik, H. J.; Zhang, W. J.; Drennan, C. L. Biochemical and Crystallographic Investigations into Isonitrile Formation by a Nonheme Iron-Dependent Oxidase/Decarboxylase. *J. Biol. Chem.* **2021**, 296, 100231.
- (32) Arya, C. K.; Ramanathan, G.; Vinothkumar, K. R.; Subramanian, R. In *Encyclopedia of Inorganic and Bioinorganic Chemistry*; John Wiley & Sons, Ltd., 2022, , 1–9.
- (33) Bassan, A.; Blomberg, M. R. A.; Borowski, T.; Siegbahn, P. E. M. Theoretical Studies of Enzyme Mechanisms Involving High-Valent Iron Intermediates. *J. Inorg. Biochem.* **2006**, *100*, 727–743.
- (34) Blomberg, M. R. A.; Borowski, T.; Himo, F.; Liao, R.-Z.; Siegbahn, P. E. M. Quantum Chemical Studies of Mechanisms for Metalloenzymes. *Chem. Rev.* **2014**, *114*, 3601–3658.
- (35) Narayan, A. R. H.; Jiménez-Osés, G.; Liu, P.; Negretti, S.; Zhao, W.; Gilbert, M. M.; Ramabhadran, R. O.; Yang, Y.-F.; Furan, L. R.; Li, Z.; Podust, L. M.; Montgomery, J.; Houk, K. N.; Sherman, D. H. Enzymatic Hydroxylation of an Unactivated Methylene C–H Bond Guided by Molecular Dynamics Simulations. *Nat. Chem.* **2015**, *7*, 653–660.
- (36) Borowski, T.; Quesne, M.; Szaleniec, M. In Advances in Protein Chemistry and Structural Biology; Karabencheva-Christova, T., Ed.; Academic Press, 2015; vol 100; pp 187–224.
- (37) Zhang, Y.; Cao, Y.; Sastri, C. V.; de Visser, S. P. Defluorination of Fluorophenols by a Heme Dehaloperoxidase: Insights into the Defluorination Mechanism. *ACS Catal.* **2025**, *15*, 3898–3912.
- (38) Bagha, U. K.; Yadav, R.; Mokkawes, T.; Satpathy, J. K.; Kumar, D.; Sastri, C. V.; de Visser, S. P. Defluorination of Fluorophenols by a Nonheme Iron(IV)-Oxo Species: Observation of a New Intermediate Along the Reaction. *Chem. Eur. J.* **2023**, *29*, No. e202300478.
- (39) Lin, Y.-T.; Ali, H. S.; de Visser, S. P. Biodegradation of Herbicides by a Plant Nonheme Iron Dioxygenase: Mechanism and Selectivity of Substrate Analogues. *Chem. Eur. J.* **2022**, 28, No. e202103982.
- (40) Neidig, M. L.; Solomon, E. I. Structure-Function Correlations in Oxygen Activating Non-Heme Iron Enzymes. *Chem. Commun.* **2005**, 5843–5863. 10.1039/b510233m
- (41) Marciesky, M.; Aga, D. S.; Bradley, I. M.; Aich, N.; Ng, C. Mechanisms and Opportunities for Rational in Silico Design of Enzymes to Degrade Per- and Polyfluoroalkyl Substances (PFAS). *J. Chem. Inf. Model.* **2023**, *63*, 7299–7319.
- (42) Austin, H. P.; Allen, M. D.; Donohoe, B. S.; Rorrer, N. A.; Kearns, F. L.; Silveira, R. L.; Pollard, B. C.; Dominick, G.; Duman, R.; El Omari, K.; Mykhaylyk, V.; Wagner, A.; Michener, W. E.; Amore, A.; Skaf, M. S.; Crowley, M. F.; Thorne, A. W.; Johnson, C. W.; Woodcock, H. L.; McGeehan, J. E.; Beckham, G. T. Characterization and Engineering of a Plastic-Degrading Aromatic Polyesterase. *Proc. Natl. Acad. Sci. U. S. A.* 2018, 115, E4350—E4357.
- (43) Jayasekara, S. K.; Joni, H. D.; Jayantha, B.; Dissanayake, L.; Mandrell, C.; Sinharage, M. M. S.; Molitor, R.; Jayasekara, T.; Sivakumar, P.; Jayakody, L. N. Trends in in-Silico Guided Engineering of Efficient Polyethylene Terephthalate (PET) Hydrolyzing Enzymes to Enable Bio-Recycling and Upcycling of Pet. Comput. Struct. Biotechnol. J. 2023, 21, 3513–3521.
- (44) Pyser, J. B.; Chakrabarty, S.; Romero, E. O.; Narayan, A. R. H. State-of-the-Art Biocatalysis. ACS Cent. Sci. 2021, 7, 1105–1116.
- (45) Kulik, H. J.; Blasiak, L. C.; Marzari, N.; Drennan, C. L. First-Principles Study of Non-Heme Fe(II) halogenase SyrB2 Reactivity. *J. Am. Chem. Soc.* **2009**, *131*, 14426–14433.
- (46) Borowski, T.; Noack, H.; Radon, M.; Zych, K.; Siegbahn, P. E. Mechanism of Selective Halogenation by SyrB2: A Computational Study. *J. Am. Chem. Soc.* **2010**, *132*, 12887–12898.
- (47) de Visser, S. P.; Straganz, G. D. Why Do Cysteine Dioxygenase Enzymes Contain a 3-His Ligand Motif Rather Than a 2His/1Asp Motif Like Most Nonheme Dioxygenases? *J. Phys. Chem. A* **2009**, *113*, 1835–1846.

- (48) Kumar, D.; Thiel, W.; de Visser, S. P. Theoretical Study on the Mechanism of the Oxygen Activation Process in Cysteine Dioxygenase Enzymes. *J. Am. Chem. Soc.* **2011**, *133*, 3869–3882.
- (49) Aluri, S.; de Visser, S. P. The Mechanism of Cysteine Oxygenation by Cysteine Dioxygenase Enzymes. *J. Am. Chem. Soc.* **2007**, *129*, 14846–14847.
- (50) Nazemi, A.; Steeves, A. H.; Kastner, D. W.; Kulik, H. J. Influence of the Greater Protein Environment on the Electrostatic Potential in Metalloenzyme Active Sites: The Case of Formate Dehydrogenase. *J. Phys. Chem. B* **2022**, *126*, 4069–4079.
- (51) Knott, B. C.; Erickson, E.; Allen, M. D.; Gado, J. E.; Graham, R.; Kearns, F. L.; Pardo, I.; Topuzlu, E.; Anderson, J. J.; Austin, H. P.; Dominick, G.; Johnson, C. W.; Rorrer, N. A.; Szostkiewicz, C. J.; Copié, V.; Payne, C. M.; Woodcock, H. L.; Donohoe, B. S.; Beckham, G. T.; McGeehan, J. E. Characterization and Engineering of a Two-Enzyme System for Plastics Depolymerization. *Proc. Natl. Acad. Sci. U. S. A.* 2020, 117, 25476–25485.
- (52) Van Stappen, C.; Deng, Y.; Liu, Y.; Heidari, H.; Wang, J.-X.; Zhou, Y.; Ledray, A. P.; Lu, Y. Designing Artificial Metalloenzymes by Tuning of the Environment Beyond the Primary Coordination Sphere. *Chem. Rev.* **2022**, *122*, *11974*–*12045*.
- (53) Kastner, D. W.; Nandy, A.; Mehmood, R.; Kulik, H. J. Mechanistic Insights into Substrate Positioning That Distinguish Non-Heme Fe(II)/A-Ketoglutarate-Dependent Halogenases and Hydroxylases. ACS Catal. 2023, 13, 2489–2501.
- (54) Kulik, H. J.; Drennan, C. L. Substrate Placement Influences Reactivity in Non-Heme Fe(II) Halogenases and Hydroxylases. *J. Biol. Chem.* **2013**, 288, 11233–11241.
- (55) Timmins, A.; Fowler, N. J.; Warwicker, J.; Straganz, G. D.; de Visser, S. P. Does Substrate Positioning Affect the Selectivity and Reactivity in the Hectochlorin Biosynthesis halogenase? *Front. Chem.* **2018**. *6*, 513.
- (56) Wojdyla, Z.; Borowski, T. Properties of the Reactants and Their Interactions within and with the Enzyme Binding Cavity Determine Reaction Selectivities. The Case of Fe(II)/2-Oxoglutarate Dependent Enzymes. *Chem. Eur. J.* **2022**, *28*, No. e202104106.
- (57) Jiang, Y.; Ding, N.; Shao, Q.; Stull, S. L.; Cheng, Z.; Yang, Z. J. Substrate Positioning Dynamics Involves a Non-Electrostatic Component to Mediate Catalysis. *J. Phys. Chem. Lett.* **2023**, *14*, 11480–11489.
- (58) Radley, E.; Davidson, J.; Foster, J.; Obexer, R.; Bell, E. L.; Green, A. P. Engineering Enzymes for Environmental Sustainability. *Angew. Chem., Int. Ed.* **2023**, *62*, No. e202309305.
- (59) Cunningham, K. M.; Shin, W.; Yang, Z. J. Computational Studies of Enzymes for C-F Bond Degradation and Functionalization. *ChemPhysChem* **2025**, 26, No. e202401130.
- (60) Pavlova, M.; Klvana, M.; Prokop, Z.; Chaloupkova, R.; Banas, P.; Otyepka, M.; Wade, R. C.; Tsuda, M.; Nagata, Y.; Damborsky, J. Redesigning Dehalogenase Access Tunnels as a Strategy for Degrading an Anthropogenic Substrate. *Nat. Chem. Biol.* **2009**, *5*, 727–733.
- (61) Floor, R. J.; Wijma, H. J.; Colpa, D. I.; Ramos-Silva, A.; Jekel, P. A.; Szymański, W.; Feringa, B. L.; Marrink, S. J.; Janssen, D. B. Computational Library Design for Increasing Haloalkane Dehalogenase Stability. *ChemBioChem.* **2014**, *15*, 1660–1672.
- (62) Shao, Q.; Jiang, Y.; Yang, Z. J. EnzyHTP: A High-Throughput Computational Platform for Enzyme Modeling. *J. Chem. Inf. Model.* **2022**, *62*, *647*–*655*.
- (63) Khersonsky, O.; Lipsh, R.; Avizemer, Z.; Ashani, Y.; Goldsmith, M.; Leader, H.; Dym, O.; Rogotner, S.; Trudeau, D. L.; Prilusky, J.; Amengual-Rigo, P.; Guallar, V.; Tawfik, D. S.; Fleishman, S. J. Automated Design of Efficient and Functionally Diverse Enzyme Repertoires. *Mol. Cell* 2018, 72, 178–186.e5.
- (64) Vinothkumar, K. R.; Arya, C. K.; Ramanathan, G.; Subramanian, R. Comparison of Cryoem and X-Ray Structures of Dimethylformamidase. *Prog. Biophys. Mol. Biol.* **2021**, *160*, 66–78.
- (65) Swaroop, S.; Sughosh, P.; Ramanathan, G. Biomineralization of N,N-Dimethylformamide by Paracoccus Sp. Strain DMF. *J. Hazard. Mater.* **2009**, 171, 268–272.

- (66) Karelina, M.; Kulik, H. J. Systematic Quantum Mechanical Region Determination in QM/MM Simulation. *J. Chem. Theory Comput.* **2017**, *13*, 563–576.
- (67) Kulik, H. J.; Zhang, J.; Klinman, J. P.; Martínez, T. J. How Large Should the Qm Region Be in QM/MM Calculations? The Case of Catechol O-Methyltransferase. *J. Phys. Chem. B* **2016**, *120*, 11381–11394.
- (68) Chi, B.; Li, F.; Wang, X.; Pan, H.; Yi, X.; Liu, Y.; Zhan, J.; Zhang, X.; Zhou, H.; Wang, W. Dmf Mineralization and Substrate Specificity Mechanism of Aminobacter Ciceronei DMFA1. *Environ. Res.* 2024, 245, No. 117980.
- (69) Chi, B.; Zou, J.; Pan, H.; Yi, X.; Liu, Y.; Zhang, X.; Zhao, Z.; Zhan, J.; Zhou, H. Elucidation of the Complete Degradation Mechanism of N,N-Dimethylformamide (DMF) and Substrate Preference within a Synthetic Bacterial Consortium (DMFsyn) Formed Via a "Top-Down" Strategy. Chem. Eng. J. 2024, 479, No. 147658.
- (70) Thom, A. J. W.; Sundstrom, E. J.; Head-Gordon, M. Loba: A Localized Orbital Bonding Analysis to Calculate Oxidation States, with Application to a Model Water Oxidation Catalyst. *Phys. Chem. Chem. Phys.* **2009**, *11*, 11297–11304.
- (71) Lu, T.; Chen, F. Multiwfn: A Multifunctional Wavefunction Analyzer. J. Comput. Chem. 2012, 33, 580-592.
- (72) Neese, F.; Wennmohs, F.; Becker, U.; Riplinger, C. The Orca Quantum Chemistry Program Package. *J. Chem. Phys.* **2020**, *152*, 224108.
- (73) Stephens, P. J.; Devlin, F. J.; Chabalowski, C. F.; Frisch, M. J. Ab-Initio Calculation of Vibrational Absorption and Circular-Dichroism Spectra Using Density-Functional Force-Fields. *J. Phys. Chem.* **1994**, 98, 11623–11627.
- (74) Lee, C. T.; Yang, W. T.; Parr, R. G. Development of the Colle-Salvetti Correlation-Energy Formula into a Functional of the Electron-Density. *Phys. Rev. B* **1988**, *37*, 785–789.
- (75) Becke, A. D. Density-Functional Thermochemistry. III. The Role of Exact Exchange. *J. Chem. Phys.* **1993**, *98*, 5648–5652.
- (76) Grimme, S.; Antony, J.; Ehrlich, S.; Krieg, H. A Consistent and Accurate Ab Initio Parametrization of Density Functional Dispersion Correction (DFT-D) for the 94 Elements H-Pu. *J. Chem. Phys.* **2010**, 132, 154104.
- (77) Becke, A. D.; Johnson, E. R. A Simple Effective Potential for Exchange. *J. Chem. Phys.* **2006**, *124*, 221101.
- (78) Li, L.; Li, C.; Zhang, Z.; Alexov, E. On the Dielectric "Constant" of Proteins: Smooth Dielectric Function for Macromolecular Modeling and Its Implementation in Delphi. *J. Chem. Theory Comput.* **2013**, *9*, 2126–2136.
- (79) Lange, A. W.; Herbert, J. M. A Smooth, Nonsingular, and Faithful Discretization Scheme for Polarizable Continuum Models: The Switching/Gaussian Approach. *J. Chem. Phys.* **2010**, *133*, 244111.
- (80) Baker, J. An Algorithm for the Location of Transition States. *J. Comput. Chem.* **1986**, *7*, 385–395.
- (81) Zhong, S.; Barnes, E. C.; Petersson, G. A. Uniformly Convergent N-Tuple-Z Augmented Polarized (nZaP) Basis Sets for Complete Basis Set Extrapolations. I. Self-Consistent Field Energies. J. Chem. Phys. 2008, 129, 184116.
- (82) Helgaker, T.; Klopper, W.; Koch, H.; Noga, J. Basis-Set Convergence of Correlated Calculations on Water. *J. Chem. Phys.* **1997**, *106*, 9639–9646.
- (83) Perdew, J. P.; Burke, K.; Ernzerhof, M. Generalized Gradient Approximation Made Simple. *Phys. Rev. Lett.* **1996**, *77*, 3865–3868.
- (84) Adamo, C.; Barone, V. Toward Reliable Density Functional Methods without Adjustable Parameters: The PBE0 Model. *J. Chem. Phys.* **1999**, *110*, 6158–6170.
- (85) Perdew, J. P.; Ernzerhof, M.; Burke, K. Rationale for Mixing Exact Exchange with Density Functional Approximations. *J. Chem. Phys.* **1996**, 105, 9982–9985.
- (86) Chai, J.-D.; Head-Gordon, M. Long-Range Corrected Hybrid Density Functionals with Damped Atom—Atom Dispersion Corrections. *Phys. Chem. Chem. Phys.* **2008**, *10*, 6615–6620.

- (87) Bader, R. F. W. A Quantum Theory of Molecular Structure and Its Applications. *Chem. Rev.* **1991**, *91*, 893–928.
- (88) Espinosa, E.; Molins, E.; Lecomte, C. Hydrogen Bond Strengths Revealed by Topological Analyses of Experimentally Observed Electron Densities. *Chem. Phys. Lett.* **1998**, 285, 170–173.
- (89) Emamian, S.; Lu, T.; Kruse, H.; Emamian, H. Exploring Nature and Predicting Strength of Hydrogen Bonds: A Correlation Analysis between Atoms-in-Molecules Descriptors, Binding Energies, and Energy Components of Symmetry-Adapted Perturbation Theory. *J. Comput. Chem.* **2019**, *40*, 2868–2881.
- (90) Fuster, F.; Grabowski, S. J. Intramolecular Hydrogen Bonds: The QTAIM and ELF Characteristics. *J. Phys. Chem. A* **2011**, *115*, 10078–10086.
- (91) Khaliullin, R. Z.; Cobar, E. A.; Lochan, R. C.; Bell, A. T.; Head-Gordon, M. Unravelling the Origin of Intermolecular Interactions Using Absolutely Localized Molecular Orbitals. *J. Phys. Chem. A* **2007**, 111, 8753–8765.
- (92) Shao, Y.; Gan, Z.; Epifanovsky, E.; Gilbert, A. T. B.; Wormit, M.; Kussmann, J.; Lange, A. W.; Behn, A.; Deng, J.; Feng, X.; Ghosh, D.; Goldey, M.; Horn, P. R.; Jacobson, L. D.; Kaliman, I.; Khaliullin, R. Z.; Kuś, T.; Landau, A.; Liu, J.; Proynov, E. I.; Rhee, Y. M.; Richard, R. M.; Rohrdanz, M. A.; Steele, R. P.; Sundstrom, E. J.; Woodcock, H. L., Iii; Zimmerman, P. M.; Zuev, D.; Albrecht, B.; Alguire, E.; Austin, B.; Beran, G. J. O.; Bernard, Y. A.; Berquist, E.; Brandhorst, K.; Bravaya, K. B.; Brown, S. T.; Casanova, D.; Chang, C.-M.; Chen, Y.; Chien, S. H.; Closser, K. D.; Crittenden, D. L.; Diedenhofen, M.; DiStasio, R. A., Jr; Do, H.; Dutoi, A. D.; Edgar, R. G.; Fatehi, S.; Fusti-Molnar, L.; Ghysels, A.; Golubeva-Zadorozhnaya, A.; Gomes, J.; Hanson-Heine, M. W. D.; Harbach, P. H. P.; Hauser, A. W.; Hohenstein, E. G.; Holden, Z. C.; Jagau, T.-C.; Ji, H.; Kaduk, B.; Khistyaev, K.; Kim, J.; Kim, J.; King, R. A.; Klunzinger, P.; Kosenkov, D.; Kowalczyk, T.; Krauter, C. M.; Lao, K. U.; Laurent, A. D.; Lawler, K. V.; Levchenko, S. V.; Lin, C. Y.; Liu, F.; Livshits, E.; Lochan, R. C.; Luenser, A.; Manohar, P.; Manzer, S. F.; Mao, S.-P.; Mardirossian, N.; Marenich, A. V.; Maurer, S. A.; Mayhall, N. J.; Neuscamman, E.; Oana, C. M.; Olivares-Amaya, R.; O'Neill, D. P.; Parkhill, J. A.; Perrine, T. M.; Peverati, R.; Prociuk, A.; Rehn, D. R.; Rosta, E.; Russ, N. J.; Sharada, S. M.; Sharma, S.; Small, D. W.; Sodt, A.; Stein, T.; Stück, D.; Su, Y.-C.; Thom, A. J. W.; Tsuchimochi, T.; Vanovschi, V.; Vogt, L.; Vydrov, O.; Wang, T.; Watson, M. A.; Wenzel, J.; White, A.; Williams, C. F.; Yang, J.; Yeganeh, S.; Yost, S. R.; You, Z.-Q.; Zhang, I. Y.; Zhang, X.; Zhao, Y.; Brooks, B. R.; Chan, G. K. L.; Chipman, D. M.; Cramer, C. J.; Goddard, W. A., Iii; Gordon, M. S.; Hehre, W. J.; Klamt, A.; Schaefer, H. F., Iii; Schmidt, M. W.; Sherrill, C. D.; Truhlar, D. G.; Warshel, A.; Xu, X.; Aspuru-Guzik, A.; Baer, R.; Bell, A. T.; Besley, N. A.; Chai, J.-D.; Dreuw, A.; Dunietz, B. D.; Furlani, T. R.; Gwaltney, S. R.; Hsu, C.-P.; Jung, Y.; Kong, J.; Lambrecht, D. S.; Liang, W.; Ochsenfeld, C.; Rassolov, V. A.; Slipchenko, L. V.; Subotnik, J. E.; Van Voorhis, T.; Herbert, J. M.; Krylov, A. I.; Gill, P. M. W.; Head-Gordon, M. Advances in Molecular Quantum Chemistry Contained in the Q-Chem 4 Program Package. Mol. Phys. 2015, 113, 184-215.
- (93) Solomon, E. I.; Decker, A.; Lehnert, N. Non-Heme Iron Enzymes: Contrasts to Heme Catalysis. *Proc. Natl. Acad. Sci. U. S. A.* **2003**, *100*, 3589–3594.
- (94) Fersht, A. R.; Requena, Y. Free Energies of Hydrolysis of Amides and Peptides in Aqueous Solution at 25.Deg. *J. Am. Chem. Soc.* 1971, 93, 3499–3504.
- (95) Cooper, W. C.; Chilukoorie, A.; Polam, S.; Scott, D.; Wiseman, F. A Comparative Study on the Hydrolysis of Acetic Anhydride and N,N-Dimethylformamide: Kinetic Isotope Effect, Transition-State Structure, Polarity, and Solvent Effect. *J. Phys. Org. Chem.* **2017**, *30*, No. e3701.
- (96) Buncel, E.; Symons, E. A. The Inherent Instability of Dimethylformamide—Water Systems Containing Hydroxide Ion. *Journal of the Chemical Society D: Chemical Communications* **1970**, *0*, 164–165. 10.1039/C29700000164

- (97) Thurlkill, R. L.; Grimsley, G. R.; Scholtz, J. M.; Pace, C. N. pK Values of the Ionizable Groups of Proteins. *Protein Sci.* **2006**, *15*, 1214–1218.
- (98) Harris, T. K.; Turner, G. J. Structural Basis of Perturbed pKa Values of Catalytic Groups in Enzyme Active Sites. *IUBMB Life* **2002**, 53, 85–98.
- (99) Reinhardt, C. R.; Kastner, D. W.; Kulik, H. J. Role of Active Site Residues and Weak Noncovalent Interactions in Substrate Positioning in N,N-dimethylformamidase, *Biochemistry*, **2025**, *64*, 2926-2937.
- (100) Afonin, A. V.; Vashchenko, A. V.; Sigalov, M. V. Estimating the Energy of Intramolecular Hydrogen Bonds from 1h Nmr and Qtaim Calculations. *Org. Biomol. Chem.* **2016**, *14*, 11199–11211.
- (101) Kastner, D. W.; Reinhardt, C. R.; Adamji, H.; Oscar-Okpala, T. S.; Kevlishvili, I.; Román-Leshkov, Y.; Kulik, H. J. Zenodo 2025.